Anomalous-x-ray-scattering study of local order in bcc $Fe_{0.53}Cr_{0.47}$

L. Reinhard,* J. L. Robertson,† and S. C. Moss
Department of Physics, University of Houston, Houston, Texas 77204-5506

G. E. Ice, P. Zschack, and C. J. Sparks
Metals and Ceramics Division, Oak Ridge National Laboratory, Oak Ridge, Tennessee 37831-6118
(Received 28 May 1991)

A single crystal of $Fe_{0.53}Cr_{0.47}$, quenched to 300 K after an anneal above the σ-phase boundary, was studied at three x-ray energies: 5.969, 7.092, and 7.6 keV (where the x-ray contrast was ~ 0). With our analyzer detector we were able to remove the Compton and resonant Raman scattering experimentally to leave solely the diffuse scattering from concentration fluctuations and atomic displacements. Using the 7.6-keV data to determine and remove the combined pure static and thermal diffuse scattering, the other two data sets were least-squares fitted for short-range order and local-atomic-displacement parameters. These data sets both indicate a clustering tendency (Fe-Fe and Cr-Cr local environments). Inverse Monte Carlo and Krivoglaz-Clapp-Moss determinations of pair-interaction energies agree well and compare favorably with recent theoretical calculations. The average individual Fe-Fe and Cr-Cr distances were also determined and revealed a contraction of both Fe-Fe and Cr-Cr nearest-neighbor distances (Cr is the larger atom). This result disagrees with a conventional treatment of atom-size effects in solid solutions and must be understood using species-dependent solute-lattice couplings. Finally, no indication of premonitory σ-phase fluctuations was found although diffuse scattering attributable to a related ω-phase softness was observed.

I. INTRODUCTION

The binary Fe-Cr system[1] exhibits a body-centered-cubic solid solution (α-Fe-Cr) in a wide temperature and concentration range. At ~ 1100 K, a structural transformation to the σ phase, a complex Frank-Kaspar phase, occurs. According to thermodynamical evaluations,[1,2] the σ phase decomposes below ~ 700 K into Fe-rich and Cr-rich bcc phases. Since the bcc-σ transformation is very sluggish, a metastable miscibility gap for α-Fe-Cr is observed well above this decomposition temperature. One might then expect the local order in the bcc phase to reveal a tendency toward phase separation. However, there is the alternative possibility that directly above the σ-phase equilibrium boundary the local atomic arrangements reflect the incipient σ-phase formation through premonitory fluctuations. In alloy systems, such premonitory fluctuations can, for example, include short-range order as well as local atomic displacements. For a quantitative investigation of short-range order and atomic displacements diffuse x-ray and neutron scattering are well suited.[3–5]

A neutron scattering study[6] on Fe-rich polycrystalline α-Fe-Cr has shown an inversion in the character of the short-range order from a preference for unlike (Cr-Fe) pairs for Cr concentrations below $\sim 9\%$ to a preference for like pairs (Fe-Fe, Cr-Cr) above this concentration. This tendency appears to be reflected as well in band-structure calculations[7] of the pair interactions responsible for the local chemical order. The clustering behavior at higher Cr concentrations is, of course, compatible with the observed miscibility gap. No diffuse-scattering measurements on α-Fe-Cr single crystals have, to our knowledge, been reported in the literature.

The present single-crystal study was selected for several reasons.

(a) We wished to explore the relationship between the local order in the bcc α-phase and atomic arrangements in the σ phase; i.e., we were interested in the possibility of premonitory σ-phase fluctuations above the σ-phase boundary;

(b) we were interested in measuring the local order in a solid solution in which the atom size disparity is quite small;

(c) we hoped to employ anomalous scattering methods with a synchrotron radiation source both to enhance the scattering contrast in our sample and to reduce this contrast essentially to zero.[8] Through a careful selection of incident energy, the Fe scattering may be made considerably stronger, equal to or somewhat weaker than the Cr scattering. (At energies well away from an absorption edge, the scattering factors for Fe and Cr, at zero scattering angle, differ by only two electrons.) These techniques were considered to be quite useful in removing average lattice effects from the diffuse scattering (pure thermal and static displacement scattering) and in evaluating the *individual* Fe-Fe and Cr-Cr displacement parameters.[9]

II. SCATTERING THEORY

The diffuse scatttering of x rays from solid solutions is caused by concentration fluctuations (short-range order) and the attendant displacements of the actual atomic positions from the sites of an ideally periodic mean lattice. An extensively used method developed by Borie and Sparks[10] to analyze the diffuse scattering intensity in-

cludes the distortion-induced scattering to second order in the displacements. The recent treatment of Dietrich and Fenzl[11] uses a cumulant expansion[12] to derive a hierarchy of intensity terms. We give here a description and comparison of the two methods as well as a discussion of the definitions and approximations we have used. Our notation is similar to that in Schweika and Haubold.[13]

For a given scattering vector $\mathbf{Q}$ ($Q=4\pi\sin\theta/\lambda$), the x-ray scattering amplitude for a binary alloy is expressed by

$$\rho(\mathbf{Q})=\sum_m (f_A\sigma_m^A e^{i\mathbf{Q}\cdot\mathbf{u}_m^A}+f_B\sigma_m^B e^{i\mathbf{Q}\cdot\mathbf{u}_m^B})e^{i\mathbf{Q}\cdot\mathbf{R}_m} . \quad (1)$$

The occupation numbers σ_m^i ($i=A,B$) are defined to be 1 if the site m is occupied by an atom i with a scattering factor f_i, and zero otherwise. The atoms are displaced by $\mathbf{u}_m^i$ from the positions of the mean periodic lattice $\mathbf{R}_m$. These displacements can be either static or dynamic in origin. From (1) we obtain the scattering intensity (in electron units per atom, N is the number of atoms):

$$I(\mathbf{Q})=\frac{1}{N}\langle\rho(\mathbf{Q})\rho^*(\mathbf{Q})\rangle$$
$$=\frac{1}{N}\sum_{\substack{mn\\ij}} f_i f_j^*\langle\sigma_m^i\sigma_n^j e^{i\mathbf{Q}\cdot(\mathbf{u}_m^i-\mathbf{u}_n^j)}\rangle e^{i\mathbf{Q}\cdot(\mathbf{R}_m-\mathbf{R}_n)} , \quad (2)$$

where $\langle\cdots\rangle$ denotes the thermal average.

In the original paper of Borie and Sparks,[10] the exponential $e^{i\mathbf{Q}\cdot(\mathbf{u}_m^i-\mathbf{u}_n^j)}$ in Eq. (2) is expanded up to the quadratic term to obtain various intensity components. As noted in Ref. 14 the effects of the thermal vibrations can better be taken into account if the total displacement $\mathbf{u}_m^i$ is separated into a static part ($\mathbf{w}_m^i$) and a dynamic part ($\mathbf{s}_m$) which is assumed to be independent of the atomic species i and uncorrelated with the static displacements. The thermal average in (2) is thus written as

$$\langle\sigma_m^i\sigma_n^j e^{i\mathbf{Q}\cdot(\mathbf{u}_m^i-\mathbf{u}_n^j)}\rangle$$
$$=\langle\sigma_m^i\sigma_n^j e^{i\mathbf{Q}\cdot(\mathbf{w}_m^i-\mathbf{w}_n^j)}\rangle\cdot\langle e^{i\mathbf{Q}\cdot(\mathbf{s}_m-\mathbf{s}_n)}\rangle . \quad (3)$$

The static displacements are now expanded to second order:

$$e^{i\mathbf{Q}\cdot(\mathbf{w}_m^i-\mathbf{w}_n^j)}\cong 1+i\mathbf{Q}\cdot(\mathbf{w}_m^i-\mathbf{w}_n^j)+\tfrac{1}{2}[i\mathbf{Q}\cdot(\mathbf{w}_m^i-\mathbf{w}_n^j)]^2 . \quad (4)$$

The dynamic part is rewritten[4]

$$\langle e^{i\mathbf{Q}\cdot(\mathbf{s}_m-\mathbf{s}_n)}\rangle\cong e^{-2M}e^{\langle(\mathbf{Q}\cdot\mathbf{s}_m)(\mathbf{Q}\cdot\mathbf{s}_n)\rangle} , \quad (5)$$

where

$$e^{-M}=\langle e^{i\mathbf{Q}\cdot\mathbf{s}_m}\rangle\cong e^{-1/2\langle(\mathbf{Q}\cdot\mathbf{s}_m)^2\rangle} \quad (6)$$

is the (thermal) Debye-Waller Factor. Equations (5) and (6) are exact if the $\mathbf{s}_m$ have a Gaussian probability distribution.[4]

Inserting (4) and (5) into (2) one obtains for the diffuse intensity (after separation of the Bragg part)

$$I_{\text{diff}}=I-I_{\text{Bragg}}=I_{\text{SRO}}+I_{\text{SE}}+I_2+I_{\text{TDS}} . \quad (7)$$

I_{SRO} is the short-range order intensity due to concentration fluctuations:

$$I_{\text{SRO}}=I_{\text{Laue}}\sum_l \alpha_l e^{-2M\phi_l}e^{i\mathbf{Q}\cdot\mathbf{R}_l} . \quad (8)$$

The α_l given by

$$\alpha_l=\frac{\langle\sigma_0^i\sigma_l^j\rangle-c_ic_j}{c_i(\delta_{ij}-c_j)}=1-\frac{P_l^{AB}}{c_B},\quad \alpha_0\equiv 1 , \quad (9)$$

are the Warren-Cowley short-range order parameters. $P_l^{AB}=\langle\sigma_0^A\sigma_l^B\rangle/c_A$ is the conditional probability of finding a B atom on site l given an A atom at the origin. (In all expressions we use translational invariance $\langle a_m b_n\rangle=\langle a_m b_{m+l}\rangle=\langle a_0 b_l\rangle$, $l=n-m$.)

The prefactor

$$I_{\text{Laue}}=c_Ac_B|\Delta f|^2,\quad \Delta f=f_A-f_B , \quad (10)$$

describes the diffuse scattering of a completely random binary alloy of concentration c_A ($c_B=1-c_A$) with no lattice distortions. The "coupling factors"

$$\phi_l=1-\frac{\langle(\mathbf{Q}\cdot\mathbf{s}_0)(\mathbf{Q}\cdot\mathbf{s}_l)\rangle}{2M} \quad (11)$$

can be evaluated using various approximations for phonon dispersion in the alloy.[4,15] From the definitions (11) and (6) one has $\phi_0=0$, i.e., the leading term in (8) ("Laue monotonic") has no Debye-Waller factor. (This result is valid for x-ray scattering, where the instantaneous pair correlation function is measured, but not for elastic diffuse neutron scattering.) Often, the approximation $\phi_l=1$ is made for $l\neq 0$.[14]

The next term in Eq. (7) is the distortion-induced "size-effect" scattering, which is linear in $\mathbf{u}_m^i$:

$$I_{\text{SE}}=I_{\text{Laue}}\mathbf{Q}\cdot\sum_l \boldsymbol{\gamma}_l e^{-2M\phi_l}e^{i\mathbf{Q}\cdot\mathbf{R}_l} . \quad (12)$$

The linear displacement parameters $\boldsymbol{\gamma}_l$ are given by

$$\boldsymbol{\gamma}_l=I_{\text{Laue}}^{-1}\sum_{ij} f_i f_j^*\langle\sigma_0^i\sigma_l^j\rangle\langle\mathbf{u}_l^{ij}\rangle , \quad (13)$$

where

$$\langle\mathbf{u}_l^{ij}\rangle=\langle\mathbf{u}_l^{ji}\rangle=\frac{\langle\sigma_0^i\sigma_l^j(-\mathbf{u}_0^i+\mathbf{u}_l^j)\rangle}{\langle\sigma_0^i\sigma_l^j\rangle} . \quad (14)$$

The $\langle\mathbf{u}_l^{ij}\rangle$ are thus the average relative displacements between two atoms, given an atom j on site l and an atom i at the origin. [We may substitute the total displacement $\mathbf{u}_l^j$ for $\mathbf{w}_l^j$ in (14), because odd moments of the vibrations $\mathbf{s}_l$ vanish.]

The existence of an average lattice $\langle \sigma_m^i \mathbf{u}_m^i \rangle = 0$ implies the following linear relation:

$$\sum_{ij} \langle \sigma_0^i \sigma_l^j \rangle \langle \mathbf{u}_l^{ij} \rangle = 0 \tag{15}$$

which can be used to express one of the three $\langle \mathbf{u}_l^{ij} \rangle$, say $\langle \mathbf{u}_l^{AB} \rangle$ as a function of the other two:

$$\langle \mathbf{u}_l^{AB} \rangle = -\frac{1}{2} \left[\frac{c_A/c_B + \alpha_l}{1-\alpha_l} \langle \mathbf{u}_l^{AA} \rangle + \frac{c_B/c_A + \alpha_l}{1-\alpha_l} \langle \mathbf{u}_l^{BB} \rangle \right] . \tag{16}$$

Inserting (16) into (12) yields

$$I_{\mathrm{SE}} = I_{\mathrm{Laue}} \mathbf{Q} \cdot \sum_l e^{-2M\phi_l} \left[\mathrm{Re} \left[\frac{f_A}{\Delta f} \right] \left[\frac{c_A}{c_B} + \alpha_l \right] \langle \mathbf{u}_l^{AA} \rangle - \mathrm{Re} \left[\frac{f_B}{\Delta f} \right] \left[\frac{c_B}{c_A} + \alpha_l \right] \langle \mathbf{u}_l^{BB} \rangle \right] e^{i\mathbf{Q}\cdot\mathbf{R}_l} . \tag{17}$$

Note that both $I_{\mathrm{SRO}} \propto |\Delta f|^2$ and $I_{\mathrm{SE}} \propto \Delta f$ vanish in the limit of zero contrast, $\Delta f = 0$.

The intensity I_2 is quadratic in both the displacements and scattering vector:

$$I_2 = I_{\mathrm{Laue}} \mathbf{Q} \otimes \mathbf{Q} \cdot \sum_l \boldsymbol{\epsilon}_l e^{-2M\phi_l} e^{i\mathbf{Q}\cdot R_l} \tag{18}$$

with

$$\boldsymbol{\epsilon}_l = I_{\mathrm{Laue}}^{-1} \sum_{ij} f_i f_j^* \langle \sigma_0^i \sigma_l^j \rangle \langle (\mathbf{w} \otimes \mathbf{w})_1^{ij} \rangle \tag{19}$$

and

$$\langle (\mathbf{w} \otimes \mathbf{w})_l^{ij} \rangle = \frac{\langle \sigma_0^i \sigma_l^j (-\mathbf{w}_0^i + \mathbf{w}_l^j) \otimes (-\mathbf{w}_0^i + \mathbf{w}_l^j) \rangle}{\langle \sigma_0^i \sigma_l^j \rangle} . \tag{20}$$

(The notation $\mathbf{a} \otimes \mathbf{b}$ stands for a 3×3 matrix with the elements $a_i b_j$.)

The thermal diffuse scattering I_{TDS} is usually calculated using the "phonon expansion," i.e., the expansion of $\exp(\langle (\mathbf{Q}\cdot\mathbf{s}_0)(\mathbf{Q}\cdot s_l) \rangle)$ from experimental lattice dynamics data and it may be subtracted from the measured intensity. The leading term in this phonon expansion, $I_{\mathrm{TDS1}} \sim Q^2$ can be formally included into I_2.

Based on the above equations several methods have been developed to extract the structural parameters (α_l, $\langle \mathbf{u}_l^{AA} \rangle, \ldots$) from a diffuse scattering experiment. The method proposed by Borie and Sparks[10] exploits the different symmetry properties of I_{SRO}, I_{SE}, and I_2 (which stem from relations like $\alpha_{-l} = \alpha_l$, $\gamma_{-l} = -\gamma_{-l}$) to separate the intensity terms from the measured data by a combinatorial procedure. The parameters are then obtained by Fourier inversion. This method assumes constant ratios $f_i/\Delta f$ and cannot extract the individual displacements $\langle \mathbf{u}_l^{AA} \rangle, \ldots$ but only the linear combinations γ_l and ε_l. The method of Georgopoulos and Cohen[16] uses the variation of $f_i/\Delta f$ in reciprocal space to extract intensities due to $\alpha_l, \langle \mathbf{u}_l^{AA} \rangle, \ldots$ at a particular point $\mathbf{Q}$ from a fit to the measured scattering at a set of points which are related to $\mathbf{Q}$ by symmetry. This procedure is repeated throughout a volume necessary to recover $\alpha_l, \langle \mathbf{u}_l^{AA} \rangle, \ldots$ via Fourier inversion. Finally, one can obtain the desired parameters by a linear least-squares fit to the data as first suggested by Williams.[17] This is the procedure that we have adopted here.

While they are widely used to analyze diffuse scattering experiments, the expressions presented above are somewhat inconsistent in their treatment of the displacements. Whereas the static displacements are expanded only to the second order, the dynamic displacements are manipulated using standard methods of the harmonic lattice theory which involve partial summations over all orders, as in Eq. (5). In the Dietrich and Fenzl[11] treatment a cumulant expansion method is used to derive the diffuse scattering intensity from a binary alloy employing correlation functions like $\langle \sigma_0^i \sigma_l^j \rangle$, $\langle \sigma_0^i \mathbf{u}_l^j \rangle$, etc. Their approach can be regarded as a consistent generalization of expressions similar to the one in Eq. (5) which are now also applied to the static displacements. It provides a systematic way to classify different scattering contributions according both to the order of the correlation functions and to their dependence on the scattering factors. An important aspect in the theory of Dietrich and Fenzl involves the displacement fields $\mathbf{u}_l^A$ and $\mathbf{u}_l^B$ which can be though of as functions of the set $\{\sigma_{n\neq l}^i\}$ of the occupation numbers. The $\mathbf{u}_l^i$ are thus defined for all l regardless of the values of σ_l^i. This permits the use of quantities such as $\langle \sigma_0^i \mathbf{u}_l^j \rangle$. (For a discussion of the cumulant expansion in x-ray scattering, see Ref. 18.)

The results of Ref. 11 can be summarized as follows. The diffuse intensity can be written as

$$I_{\mathrm{diff}} = S_{\mathrm{I}} + S_{\mathrm{II}}^1 + S_{\mathrm{II}}^2 . \tag{21}$$

The leading terms in S_{I} contain two-point correlations between displacements: $\langle \mathbf{u}_0^i \otimes \mathbf{u}_l^j \rangle$. S_{I} can be therefore regarded as the "pure" displacement intensity. S_{II}^2 is dominated by occupation-displacement correlations $\langle \sigma_0^i \mathbf{u}_l^j \rangle$, i.e., it is linear in the displacements, similar to I_{SE} of the Borie-Sparks theory. S_{II}^1 contains $\langle \sigma_0^i \sigma_l^j \rangle - c_i c_j$ and, neglecting certain higher order terms one can identify

$$S_{\mathrm{II}}^1 = I_{\mathrm{SRO}} . \tag{22}$$

Neglecting similar terms in S_{II}^2 yields

$$S_{\mathrm{II}}^2 = I_{\mathrm{Laue}} \mathbf{Q} \cdot \sum_l e^{-2M\phi_l} \left[\mathrm{Re} \left[\frac{f_A}{\Delta f} \right] \left[\frac{2c_A}{c_B} \right] \langle \bar{\mathbf{u}}_l^{AA} \rangle - \mathrm{Re} \left[\frac{f_B}{\Delta f} \right] \left[\frac{2c_B}{c_A} \right] \langle \bar{\mathbf{u}}_l^{BB} \rangle \right] e^{i\mathbf{Q}\cdot\mathbf{R}_l} \tag{23}$$

with

$$\langle \bar{\mathbf{u}}_l^{ij} \rangle = \frac{\langle \sigma_0^i \mathbf{u}_l^j \rangle}{c_i} \quad . \tag{24}$$

Comparing Eqs. (23) and (17) one finds an identical dependence on the scattering vector **Q** and the scattering factors f_A, f_B, with only the coefficients of the Fourier series being different. The $\langle \bar{\mathbf{u}}_l^{ij} \rangle$ contain a two-point correlation (a product of an occupation number and a displacement) similar to the α_l (two occupation numbers). The $\langle \mathbf{u}_l^{ij} \rangle$ are three-point correlations.

[Note: The theory of Dietrich and Fenzl leads to species-dependent Debye-Waller factors (static and dynamic) e^{-M_A}, e^{-M_B}. Since it is very difficult to obtain the individual e^{-M_A} and e^{-M_B} in a disordered system, we have used an overall e^{-M} in the data evaluation which is reflected in the equations. Given the small mass disparity between Fe and Cr, this should be a good approximation for the thermal Debye-Waller factor. The static DWF is negligible (see Sec. IV D). The particular approximations and assumptions employed to obtain (22) and (23) from the results in Ref. 11 were (using our notation)

(i) the Debye-Waller factors for A and B are set equal,

(ii) the quantities $E_{mi,nj}$ in Ref. 11 are approximated by $e^{\langle (\mathbf{Q}\cdot\mathbf{u}_m^i)(\mathbf{Q}\cdot\mathbf{u}_n^j) \rangle}$ which in turn are assumed to be both independent of i,j and dominated by dynamic displacements to which Eq. (5) applies,

(iii) all correlations, other than $\langle \sigma_m^j \sigma_n^j \rangle$, $\langle \sigma_m^i \mathbf{u}_n^j \rangle$, and their products with $E_{mi,nj}$, are neglected, and

(iv) $\langle \sigma_m^i e^{i\mathbf{Q}\cdot\mathbf{u}_m^j} \rangle \cong \langle e^{i\mathbf{Q}\cdot\mathbf{u}_m^j} \rangle \langle \sigma_m^i \rangle$.]

S_{I} contains all the displacement scattering not included in S_{II}^2, in particular I_{TDS}, I_2, and higher orders neglected in the Borie-Sparks treatment. The leading term in S_{I} is proportional to Q^2. As one can easily show there are two limiting cases [within the approximation (iv)], in which S_{I} is proportional to the "mean lattice scattering" $|\bar{f}|^2 = |c_A f_A e^{-M_A} + c_B f_B e^{-M_B}|^2$:

(a) The quadratic ($\langle \mathbf{u}_0^i \otimes \mathbf{u}_l^j \rangle$) and higher correlations in the displacements are independent of the atomic species i and j. This implies $M_A = M_B$.

(b) The scattering factors are equal, i.e., $f_A e^{-M_A} = f_B e^{-M_B}$.

As discussed previously, condition (a) is nearly satisfied in our sample. Requirement (b) is also reasonably well fulfilled, because $f_{\mathrm{Fe}} \approx f_{\mathrm{Cr}}$. Hence, to a good approximation, S_{I} scales with $|\bar{f}|^2$. [Of course, as we tune to absorption edges to alter the contrast, (b) will be less well satisfied.]

While the Dietrich-Fenzl development provides a more formal treatment of the complex displacement effects and considerable insight into the separation of intensities that we employ in this paper, we shall nonetheless express our results in terms of the Borie-Sparks displacement parameters. We do so because the physical significance of the parameters in Eq. (14) is more transparent than for those given in Eq. (24). A more detailed comparison of these two treatments is beyond the scope of this paper and will be presented elsewhere.

III. EXPERIMENTAL

The single crystal sample was grown at the Materials Preparation Center, Ames Laboratory, Iowa State University by Jones using a Bridgman technique. The purity of the alloying elements was 99.95% and 99.996% for Fe and Cr, respectively. The Cr concentration, as determined by chemical analysis was 47.2 at. % Cr with a homogeneity better than 0.3% over the irradiated crystal volume in the experiment. The crystal was cut with a SiC saw to obtain a surface of ~ 1 cm^2 with a normal close to the $\langle 421 \rangle$ direction, chosen to permit access to the three high symmetry directions with minimum tilting. The surface was then mechanically polished and electroetched in order to reduce surface damage. After a homogenization anneal at 1600 K the crystal was held at 1108 K (5 K above the σ-phase transition temperature[1]) for 4 days in a sealed quartz tube under a purified argon atmosphere and water quenched. It is important to note here, at the outset, that extensive small-angle neutron scattering studies[19] of quenched and annealed α-Fe-Cr alloys indicate that such a quench will essentially preserve the high temperature equilibrium configurational order.

The x-ray scattering experiment was performed on the ORNL beamline X14 (Ref. 20) of the National Synchrotron Light Source (NSLS). The essential features of the beam optics are a vertically focusing mirror[21] and a fixed-exit Si(111) monochromator consisting of a flat crystal and a sagitally bent crystal to focus the beam in the horizontal plane.[20] The sample was mounted on a four-circle diffractometer (Huber 5010). Air scattering was minimized by an evacuated hemispherical Be dome and He filled beam paths. The primary beam intensity was monitored by an ion chamber. The beam scattered from the sample was energy analyzed using a mosaic graphite (002) crystal in parafocusing geometry together with a linear position-sensitive proportional counter from which we obtained a multichannel display of the energy spectrum. This spectrometer has been described in detail elsewhere.[22] The achievable energy resolution is mainly determined by the size of the irradiated spot on the sample surface and can therefore be improved—at the expense of intensity—by reducing the size of the incident beam. Typically, the resolution varied between 20 and 50 eV FWHM, depending on the incident energy, the position in the reciprocal space, and the choice of incident beam slits. The energy analysis here is used to isolate the relatively weak diffuse scattering signal from the inelastic background, i.e., the Compton and, in particular, the resonant Raman scattering[23] (RRS). The RRS is enhanced when the incident x-ray energy is only slightly below an absorption edge; unless eliminated experimentally, it must be estimated using rather inaccurate approximations.[24]

The measurements were done using three different energies of the incident x rays.

(a) $E = 5.969$ keV (20 eV below the measured Cr K absorption edge). This energy was chosen to maximize the scattering contrast $|\Delta f|$ between Cr and Fe and thus to enhance the contribution of the short-range order scattering; we refer to it as the "Cr edge."

(b) $E=7.092$ keV (20 eV below the measured Fe K absorption edge). At this energy $\mathrm{Re}(f_{\mathrm{Cr}})>\mathrm{Re}(f_{\mathrm{Fe}})$, i.e., Cr becomes a stronger scatterer than Fe and we shall refer to it as the "Fe edge." This contrast inversion affects the sign of I_{SE} [see Eq. (17)]. Therefore, a comparison of the data measured with the "Fe edge" energy with those measured with the "Cr edge" energy highlights the size-effect scattering.

(c) $E=7.600$ keV. This choice minimizes the scattering contrast, whereby the short-range order and size effect contributions to the scattering are small, and the measured intensity is thus predominantly due to S_{I}, i.e., to TDS and higher-order static displacement scattering (other than I_{SE}).[8]

Figure 1 shows the range of contrast variation obtained in our experiment. Note the greatly enhanced $|\Delta f|^2$ at the "Cr edge," as compared with $|\Delta Z|^2=4$ without anomalous dispersion corrections, and the small $|\Delta f|^2$ for $E=7.6$ keV.

The scattering factors f_0 were taken from Ref. 25. For the anomalous scattering corrections Cromer-Liberman values[26] were used, except when the incident energy was close to the absorption edge of a particular element, i.e., in the case of $f'_{\mathrm{Cr}}, f''_{\mathrm{Cr}}$ at 5.969 keV and $f'_{\mathrm{Fe}}, f''_{\mathrm{Fe}}$ at 7.092 keV. These numbers were obtained experimentally by measuring the energy-dependent absorption of a thin foil with the same composition as the sample. From the absorption we calculated f'' using the optical theorem and f' via the Kramers-Kronig relation using a method similar to the one described in Ref. 27. Table I shows the obtained results, together with theoretical values.[26]

The diffuse intensity was measured throughout a volume in reciprocal space defined by $h_1\geq h_2\geq h_3\geq 0$. This volume covers $\frac{1}{48}$ of the solid angle. The range for the magnitude of the scattering vector [in reciprocal lattice units, $h=(a/2\pi)Q$] was $0.25\leq h\leq 2.7$ for the "Cr edge" energy and $0.25\leq h\leq 3.0$ for the two other x-ray

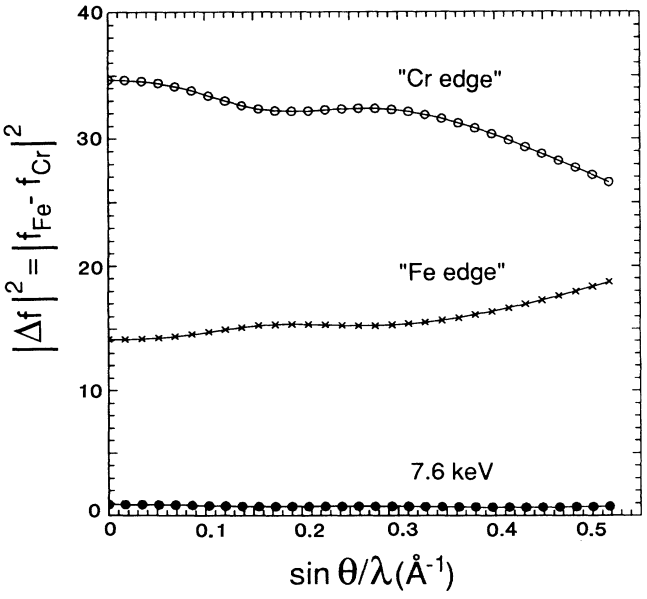

FIG. 1. $|\Delta f|^2$ as a function of $\sin\theta/\lambda$ for the three energies used.

TABLE I. Real (f') and imaginary (f'') parts of the dispersion corrections to the x-ray scattering factors used in this experiment as measured here and calculated by Sasaki (Ref. 26).

		Measurement	Ref. 26
f'_{Cr}	5.969 keV	−5.572	−5.564
f''_{Cr}	5.969 keV	0.433	0.459
f'_{Fe}	7.092 keV	−5.572	−5.688
f''_{Fe}	7.092 keV	0.454	0.470

energies. The mesh interval used was $\Delta h=0.1$ in general and $\Delta h=0.05$ for selected linear scans and small scattering angles ($h\leq 0.6$).

The raw data were corrected for surface roughness and partial passing of the beam at the sample using the variation of the K_α^{Cr} and K_α^{Fe} fluorescence with scattering vector. However, this correction was rather small and only significant for scattering angles $2\theta<20°$. For the conversion into absolute (electron) units, the integrated intensities of 5 Bragg peaks from a compacted Ni powder standard were used at each energy following a procedure outlined in Ref. 28.

IV. RESULTS AND DISCUSSION

A. Energy spectra

Figure 2 shows typical energy-resolved spectra for the "Fe edge" and the 7.6-keV measurements. (The results for the "Cr edge" energy are similar to those at the "Fe edge.") the spectrum at the "Fe edge" consists of three different contributions: the resolution broadened elastic intensity, the Fe $K-M_{\mathrm{II,III}}$ RRS with an onset 53.2 eV below the elastic line (this corresponds to the $M_{\mathrm{II,III}}$ binding energy in iron[29]), and the Compton scattering which is superimposed on the RRS. At 7.6 keV there is no RRS and the Compton scattering can therefore be seen more clearly. The dashed lines in Fig. 2 represent fits to the RRS and elastic scattering together with a calculation of the double-differential Compton cross section $(d^2\sigma/d\Omega\, d\omega)^C$. The elastic intensity was fitted with a Gaussian, the width of which defined the energy resolution used in the convolution with the calculated RRS and Compton scattering. The energy dependent efficiency of the analyzer, determined by the mosaic of the graphite crystal (0.8° FWHM), was also taken into account. To fit the RRS, a truncated Lorentzian was used, following an approximation to the relevant part of the Kramers-Heisenberg formula.[24] The Compton double-differential cross section was calculated in the impulse approximation[30] using Hartree-Fock Compton profiles for the Fe and Cr atoms from Ref. 31. In employing the impulse approximation, only contributions of electrons with binding energies smaller than the energy transfer were considered.

Within this separation scheme the desired elastic intensity is obtained from the area under the Gaussian curve. However, the applicability of the method was somewhat restricted by the accuracy of the calculated Compton cross section. For small scattering vectors ($h\leq 1.3$) the

calculated scattering significantly overestimated the measured inelastic intensity. (This was inferred from the 7.6-keV data with no RRS present.) For an intermediate range of scattering vectors the agreement was quite satisfactory [see Fig. 2(a)], but for $h \geq 2.6$ the calculation systematically underestimated the measured Compton intensities. There are two probable reasons for these discrepancies: (a) the momentum distributions in Ref. 31 are calculated for free atoms and of course do not reflect the actual band structure of the alloy; (b) the impulse approximation describes a one-particle process; for low energy and momentum transfer, however, many-body effects (plasmon excitations) may dominate the inelastic cross section.[30,32]

The underestimation of the measured Compton scattering by our calculation for large scattering vectors was not critical for the evaluation of the elastic intensity since in this range of momentum transfer the Compton and elastic scattering are well separated in energy and

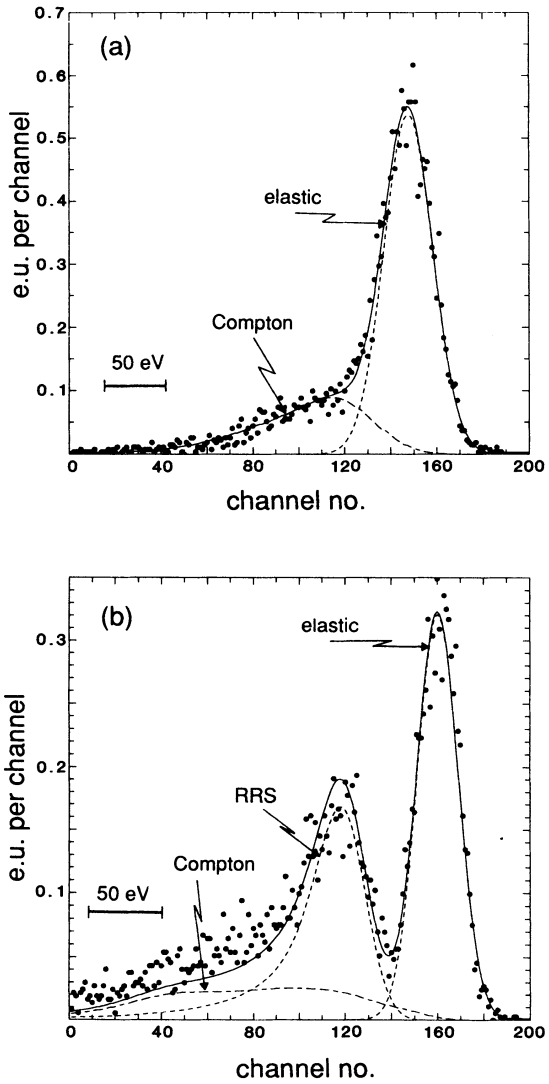

FIG. 2. Energy-resolved spectra as obtained from the position sensitive detector. (a) $\mathbf{h}=(1.7,0,0)$ at $E=7.6$ keV, (b) $\mathbf{h}=(2.8,0,0)$ at the "Fe edge" ($E=7.092$ keV). e.u. is electron units.

therefore overlap only slightly, even with our experimental energy resolution. On the other hand, because of the small Compton energy shifts at low scattering angles, the overestimation of the $(d\sigma/d\Omega\, d\omega)^C$ in the region $h \leq 1.5$ was more troublesome even though the energy-integrated Compton intensity $(d\sigma/d\Omega)^C$ is low. As a consequence we decided to use a somewhat heuristic algorithm to extract the elastic intensity for small scattering angles. Since both Compton and RRS are energy-loss processes, the "high-energy half" of the resolution-broadened elastic line will clearly be less affected by those inelastic contributions. The entire elastic part of the spectrum was therefore recovered from its "high-energy half" by reflection at the position of zero energy transfer, i.e., we calculated the following sum over the MCA channels:

$$I = 2 \sum_{n > n_0} I_n + I_{n_0} , \tag{25}$$

where n_0 is the channel number which corresponds to the center of the elastic peak.

In the final data evaluation we applied this "reflection" procedure for $h \leq 1.6$, whereas for $h > 1.6$ the aforementioned fit was used. As a consistency check we employed the "reflection" algorithm for all data points. The SRO and displacement parameters thus obtained were within the statistical 3σ error bars of the parameters obtained using "reflection" only for $h \leq 1.6$. Although the results did not depend significantly on the method applied for $h > 1.6$, we preferred to use the more elaborate fit algorithm because the "reflection" introduces an additional statistical error as it uses only half of the total elastic data (at best).

B. Experimental diffuse intensities

Figure 3 shows the experimental intensities in electron units per atom in the $(h_1,h_2,0)$ plane for the three energies used. As the Bragg peaks have already been removed from the data, the rise of intensity near the Bragg positions may be attributed to the diffuse scattering. The plots exhibit intensity ridges in $\langle 1\bar{1}0 \rangle$ directions connecting the 110 and 200 reflections as well as the 220 and 310 reflections (the latter ridge could not be measured at the "Cr edge" because of the limited Q range at this energy). Since these structures appear also at the low-contrast energy 7.6 keV, they cannot be explained by the short-range order or size effect intensity. Such ridges are indeed quite common in bcc alloys (e.g., in β brass,[33] NiAl[34]); they have been attributed to the softening of the $[110]:\langle 1\bar{1}0 \rangle$ phonon mode, i.e., of the $(c_{11}-c_{12})/2$ shear constant.[35] The intensity of the ridge connecting 220 ad 310 is larger than the one of the ridge connecting 110 and 200, because of the $\propto Q^2$ dependence of S_I.

There is an increase of intensity near the origin of the reciprocal space. The increase is more pronounced at the "Cr edge" than at the "Fe edge" and almost nonexistent at 7.6 keV. This contrast dependence as well as its location near (000) where the displacement effects are small, both clearly indicate that the increase is due to I_{SRO}. Since there is no other structure in the data with a similar

contrast dependence we conclude that I_{SRO} peaks at (or close to) (000), which in turn implies a clustering tendency. The variation of the intensity increase near the origin with the incident x-ray energy is even more apparent in the linear $\langle h00 \rangle$ scan [Fig. 4(a)]. Also in Fig. 4(a) one sees a pronounced difference between the "Cr edge" and the "Fe edge" intensity close to the (100) position. Whereas the slope of the "Cr edge" intensity is positive around (100), the slope of the "Fe edge" intensity is negative. This is clearly related to the change of sign of I_{SE} caused by the contrast inversion at the "Fe edge."

Figure 4(b) shows the measured intensity along the $\langle hhh \rangle$ line. The 7.6-keV measurement exhibits maxima in the vicinity of $\frac{2}{3}(111)$ and $\frac{4}{3}(111)$, the intensity at $\frac{4}{3}(111)$ being higher than at $\frac{2}{3}(111)$, in accordance with the Q^2 behavior which dominates S_I. This scattering pattern is quite common in bcc metals and may be related to ω-phase formation which we discuss below. The $\sim\frac{2}{3}(111)$ peak in the "Fe edge" scan is more pronounced than in the 7.6-keV scan, but the peak at $\sim\frac{4}{3}(111)$ in the "Fe edge" data is very weak. By changing the x-ray energy from the "Fe edge" to the "Cr edge," the $\frac{4}{3}(111)$ maximum regains intensity whereas the $\frac{2}{3}(111)$ peak weakens and shifts toward smaller h. The $\frac{2}{3}(111)$ maximum at the "Cr edge" is obviously affected by the strong I_{SRO} intensity near the origin, but all other intensity variations are evidently caused by the size effect scattering, since I_{SRO} is symmetric around (111) and the prefactor $|\bar{f}|^2$ for the pure displacement scattering does not change drastically with the incident x-ray energy. The redistribution of intensity between the $\frac{2}{3}(111)$ and the $\frac{4}{3}(111)$ maxima by contrast inversion is thus an interesting example of the size effect in a region of reciprocal space where the short-

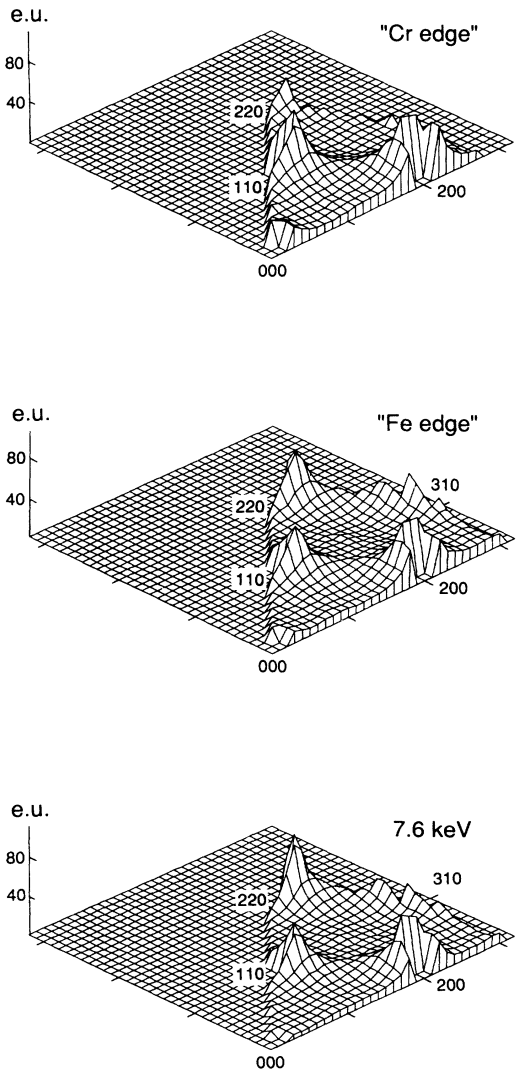

FIG. 3. Experimental intensities in electron units in the $(h_1,h_2,0)$ plane.

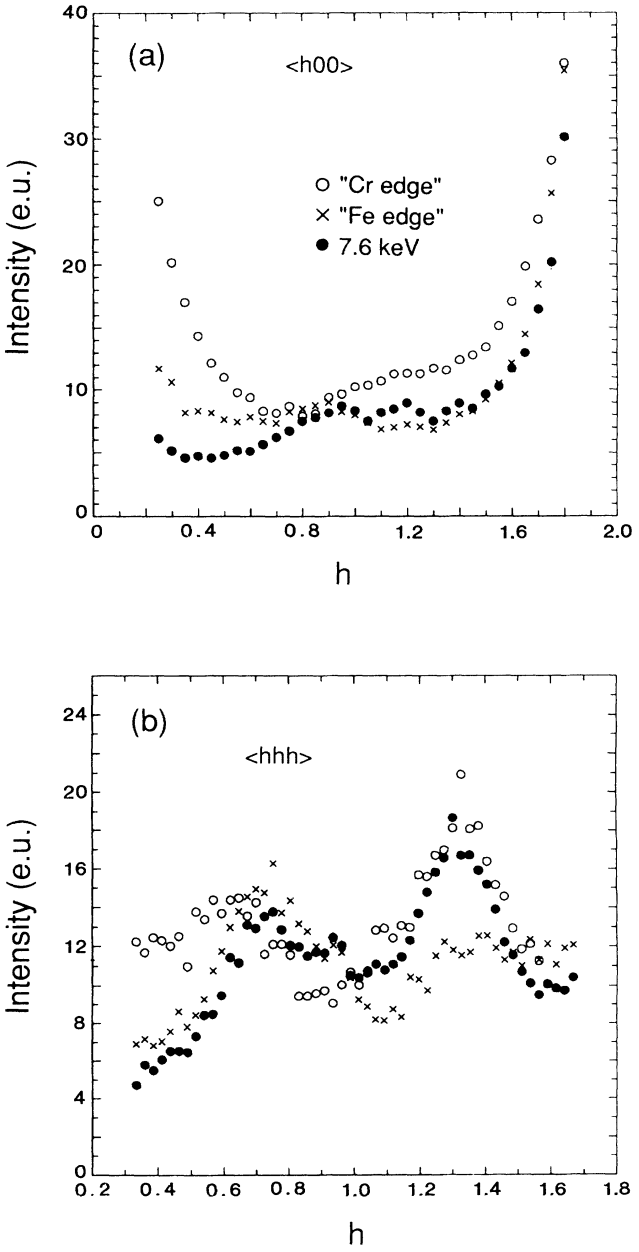

FIG. 4. Experimental intensities in electron units (a) in the $\langle h00 \rangle$ direction, (b) in the $\langle hhh \rangle$ direction.

range order intensity, as we shall see, does not vary too rapidly.

C. ω phase, central peaks, and the size effect

The maxima near $\frac{2}{3}(111)$ and equivalent points [such as $\frac{4}{3}(111)$] may be associated with an intrinsic softness of the bcc lattice to longitudinal displacements with the wave vector $\frac{2}{3}(111)$. The $\frac{2}{3}(111)$ longitudinal phonon moves two out of three consecutive 111 lattice planes toward each other, leaving the position of the third plane unchanged.[36] This displacement mode is formally related to the ω-phase transformation,[36] since one can obtain the hexagonal ω phase from the bcc lattice by collapsing 2 out of 3 $(111)_{bcc}$ planes into one $(0001)_{\omega}$ plane. Figure 5(a) shows the $[111]_L$ phonon dispersion in our sample.[37] The softening of the phonon frequencies in the vicinity of $\frac{2}{3}(111)$, typical for many bcc systems, is clearly visible. The lattice vibrations with wave vectors in the vicinity of $\frac{2}{3}(111)$ thereby have larger amplitudes and the TDS intensity will be enhanced. (In the harmonic approximation I_{TDS1} is proportional to the inverse square of the phonon frequency.[4]) Since the response function of the lattice is "soft" for wave vectors near $\frac{2}{3}(111)$ we can also expect that the (longitudinal) microscopic stresses associated with the difference in the atomic sizes will preferably induce static displacements with these spatial frequencies. Figure 5(b) shows that the neutron *elastic* diffuse scattering[37] (const-ω scan for an energy transfer $\omega=0$) peaks near $\frac{4}{3}(111)$. All inelastic contributions outside the energy resolution window (≈ 1.5 meV FWHM) are removed in this scan.

It is interesting to note that some bcc phases of pure elements, such as β-Ti and β-Zr, also exhibit $\frac{2}{3}(111)$ maxima in const-$\omega=0$ scans.[38] These maxima have been attributed not to truly elastic scattering, but to overdamped $\frac{2}{3}(111)$ longitudinal phonons, with a nonzero center frequency, which give a large quasielastic scattering when sampled within the resolution volume in Q-ω space.[38] An overdamped phonon response has also been observed in some bcc alloys (e.g., in Nb-Zr[39,40]) but contrary to the situation in pure elements, a resolution limited "central peak" with a maximum around $\frac{2}{3}(111)$ has been seen on top of the broadened inelastic intensity. However, all $[111]_L$ phonons that we measured were reasonably well defined in energy, and we therefore expect the $\frac{4}{3}(111)$ peak in Fig. 5(b) to be dominated by genuine elastic intensity caused by static displacements. This is further confirmed by the existence of the size effect scattering in Fig. 4 since purely dynamical displacements can not give rise to a size effect intensity. Hence, the peaks in the x-ray intensity [Fig. 4(b)] contain not only TDS but also a static component. Conversely, the existence of static "pure displacement" intensity requires there to be size effect scattering.

The relation between the static part of S_I and the size effect term can be shown using Krivoglaz' approximate expression for the diffuse scattering intensity[3] (in the notation of Sec. II):

$$I_{\text{diff}}=c_A c_B \alpha(\mathbf{Q})|\Delta f-\bar{f}\mathbf{Q}\cdot\mathbf{A}(\mathbf{Q})|^2 . \quad (26)$$

$\alpha(\mathbf{Q})$ and $\mathbf{A}(\mathbf{Q})$ are the Fourier transforms of the SRO parameters and the quantities $\mathbf{A}_{mn}$, respectively. The $\mathbf{A}_{mn}$ linearly couple the static displacement field (which is assumed here to be independent of the atomic species) to the concentration fluctuations:

$$\mathbf{w}_m=\sum_n \mathbf{A}_{mn}\Delta\sigma_n^A, \quad \Delta\sigma_n^A=\sigma_n^A-c_A=-\Delta\sigma_n^B . \quad (27)$$

The term $\sim|\Delta f|^2$ in Eq. (26) gives the short-range order scattering, while the cross term leads to the size effect

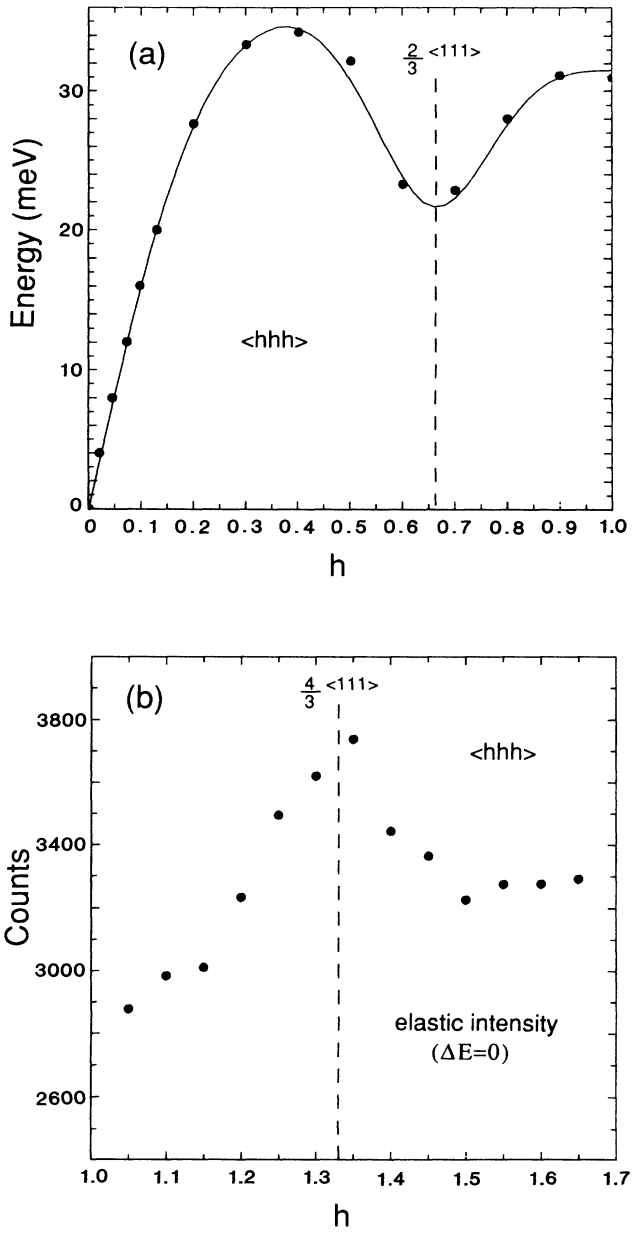

FIG. 5. (a) Measured $[111]_L$ phonon dispersion. The solid line indicates a fit to a 5 neighbor Born-von Karman model; (b) diffuse elastic neutron scattering intensity in the $\langle hhh \rangle$ direction.

scattering. The term $\propto |\mathbf{A}|^2$ corresponds to the quadratic displacement intensity. If $|\mathbf{A}|^2$, and thus the pure displacement scattering, is large, the size effect intensity, $\propto \mathbf{A}$, must also be enhanced regardless of the value of the short-range order intensity. Figure 5(b) therefore contains both contributions. In Fig. 4 one also expects strong size effect scattering ($\propto \mathbf{A}$) near $\frac{2}{3}(111)$ and $\frac{4}{3}(111)$ unless the contrast Δf is small, as in the 7.6-keV measurement.

D. Data evaluation

The normalized scattering intensities at the three energies were used to obtain short-range order parameters and the individual (Cr-Cr, Fe-Fe) linear displacement parameters. In a first step, an estimated value for the S_I intensity was subtracted from the "Cr edge" and the "Fe edge" data. This estimate was given by the measured intensities at 7.6 keV scaled with the "mean lattice scattering" $|\bar{f}|^2$:

$$S_I \approx \frac{|\bar{f}|^2}{|\bar{f}|^2_{7.6\text{ keV}}} I_{7.6\text{ keV}} \cdot \tag{28}$$

After subtraction of S_I, given by Eq. (28), the "Cr edge" and the "Fe edge" data contain to a good approximation only the short-range order and the size effect intensities. A least-squares fit to this data at both energies was then employed to obtain the α_l and the $\langle \mathbf{u}_l^{\mathrm{CrCr}} \rangle$, $\langle \mathbf{u}_l^{\mathrm{FeFe}} \rangle$ according to Eqs. (8) and (17).

For this fit, the thermal mean-square displacement $\langle \mathbf{s}_l^2 \rangle$ in the thermal Debye-Waller factor $2M^{\mathrm{th}} = \frac{1}{3}Q^2 \langle \mathbf{s}_l^2 \rangle$ was calculated from the elastic constants as obtained from our phonon dispersion curves[37] ($c_{11} = 2.56 \times 10^{11}$ Nm^{-2}, $c_{12} = 1.10 \times 10^{11}$ Nm^{-2}, $c_{44} = 1.11 \times 10^{11}$ Nm^{-2}) using the method of Quimby and Sutton.[41] The static mean-square displacement was estimated[3] from the elastic constants and the concentration (Cr) dependence of the lattice parameter $1/a\,(da/dc) = 4.57 \times 10^{-3}$ (Ref. 42). The RMS values thus obtained were $\langle \mathbf{s}_l^2 \rangle^{1/2} = 0.099$ Å and $\langle \mathbf{w}_l^2 \rangle^{1/2} = 0.0028$ Å. Hence the RMS static displacement amounts only to $\sim 3\%$ of the RMS thermal displacement. The factors ϕ_l [Eq. (11)] were calculated assuming linear dispersion as outlined in Ref. 4.

In a refinement step the SRO and size effect parameters, obtained as described above, were used to calculate the SRO and size effect intensities at 7.6 keV; these intensities were then subtracted from the measured 7.6-keV data to lead to a better estimate for S_I. The "Cr edge" and the "Fe edge" data were again corrected for S_I and from a subsequent least-squares fit we obtained a final set of 21 SRO parameters and 9 pairs of Fe-Fe and Cr-Cr displacement parameters. Including more parameters in the fit did not significantly improve the χ^2 value (~ 4.2) and did not change the values of the previous parameters.

In the present evaluation, all data points with a distance $\Delta h \geq 0.2$ from the Bragg reflections were considered. However, the results were also stable with respect to variations in the volume around the fundamentals excluded from the fit, up to $\Delta h \approx 0.5$. It has to be emphasized that the least-squares method, as opposed to Fourier analysis of data obtained by "separation methods," does not require any extrapolations under the Bragg positions which might be troublesome for clustering systems.

The final parameters are listed in Tables II and III. The errors given are based solely on counting statistics. All quantities are labeled with the three-dimensional shell index (l,m,n). The displacement parameters $\langle \mathbf{u}_{lmn}^{ij} \rangle$ are given in terms of their x components (along the l direction), $\langle x_{lmn}^{ij} \rangle$. Other components follow from cubic symmetry. All displacements are in units of the lattice parameter $a = 2.876$ Å (Ref. 42). We should also note here, for the experts, that the value of α_{000} is 1.18 rather than 1.00 as it ought formally to be if the normalization is correct and all sources of significant (and parasitic) intensity have been accounted for (or removed). We believe our normalization method to be accurate to within 5% and we thus attribute the reported small deviation in α_{000} to errors in Compton and RRS removal and to residual S_I that was not completely eliminated in our zero contrast subtraction (despite the successive cyclings noted earlier). This S_I contaminant consists mainly of TDS which certainly does not contribute a flat background. However, the precautions taken in varying the volume sampled near Bragg peaks convinced us that the most sensible procedure was to leave this dc term (α_{000}) alone and report the other parameters as is.

Figure 6 compares the measured intensities in the $(h_1,h_2,0)$ plane (after subtraction of S_I) with those reconstructed from the obtained parameters. The increase of the intensity near the Bragg positions and the details of the intensity modulations in the *zwischenreflex* region are well reproduced. These modulations are largely due to the size effect scattering as can be inferred from

TABLE II. Short-range order parameters, α_{lmn}.

lmn	α_{lmn}
000	1.1806(23)
111	0.1596(14)
200	0.0691(14)
220	0.0455(11)
311	0.0271(10)
222	0.0253(11)
400	0.0036(11)
331	0.0074(8)
420	0.0074(7)
422	0.0043(7)
333	0.0051(8)
511	0.0025(6)
440	−0.0006(7)
531	0.0016(4)
442	0.0022(5)
600	−0.0020(8)
620	0.0009(4)
533	0.0009(4)
622	0.0010(4)
444	0.0007(7)
551	−0.0002(4)

TABLE III. Displacement parameters $\langle x^{ij}_{lmn} \rangle$, the x components of $\langle \mathbf{u}^{ij}_{lmn} \rangle$. The $\langle x^{\mathrm{FeCr}}_{lmn} \rangle$ were obtained from Eq. (16).

lmn	$\langle x^{\mathrm{FeFe}}_{lmn} \rangle$	$\langle x^{\mathrm{CrCr}}_{lmn} \rangle$	$\langle x^{\mathrm{FeCr}}_{lmn} \rangle$
111	−0.000 70(4)	−0.001 90(5)	0.001 72(4)
200	−0.000 29(9)	0.002 68(12)	−0.001 20(8)
220	−0.000 22(4)	−0.000 50(6)	0.000 38(4)
311	0.000 18(5)	0.000 07(6)	−0.000 13(4)
131	−0.000 22(3)	0.000 11(4)	0.000 08(2)
222	−0.000 53(5)	0.000 39(6)	0.000 13(4)
400	0.000 09(9)	0.000 63(13)	−0.000 34(8)
331	−0.000 13(4)	0.000 16(4)	0.000 00(5)
133	−0.000 05(4)	−0.000 05(6)	0.000 05(4)

the systematic differences between the "Cr edge" and the "Fe edge" data (e.g., the "dip" near 210 at the "Cr edge" which becomes a local maximum at the "Fe edge," both of which may be related to a measurable zone boundary softness in the $[100]_L$ phonon branch[37]).

A set of measured intensities is compared with the fitted intensities along the $\langle hhh \rangle$ direction in Fig. 7. The intensity minimum around $h=0.8$ at the "Cr edge" and the maximum around $h=0.7$ at the "Fe edge" are caused by the size effect modulation and may nominally be related to a peak at $\frac{2}{3}(111)$ in the elastic neutron scattering. The difference in their positions can be explained with the SRO intensity which peaks at the origin, $h=0$, and therefore will shift a size effect-induced minimum toward a higher h value, whereas a maximum will be shifted toward a lower h. The same arguments apply to the maximum around 1.35 at the "Cr edge" and the 1.2 minimum at the "Fe edge," which are directly related to the maximum of S_{I} close to $\frac{4}{3}(111)$. (Nearly all of the "Cr edge" data seem to lie below the fitted curve but otherwise follow it closely. This linear scan, however, was taken at the end of our run and therefore was not normalized in the same way as the full data set from which the fitted curve was obtained. In fact, using only the full data set, the experimental points, while more sparsely distributed, did not deviate from the fitted curves in any systematic way.)

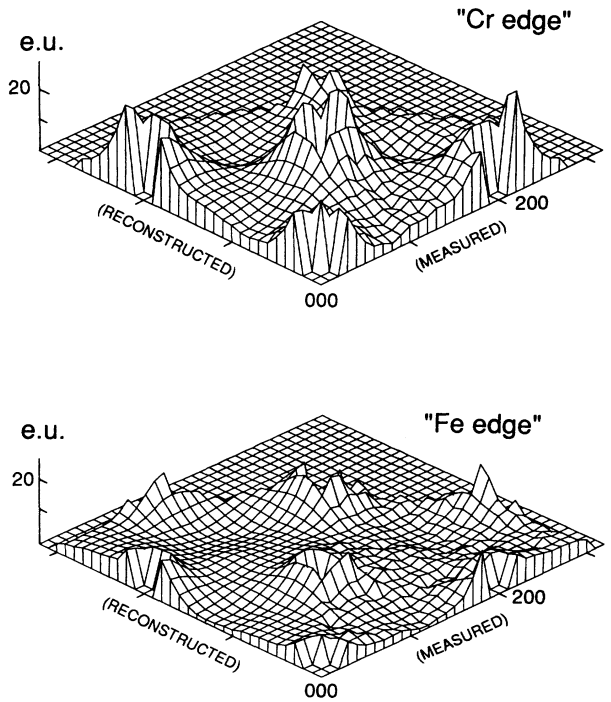

FIG. 6. Measured and reconstructed intensities in the $(h_1,h_2,0)$ plane in electron units for the "Cr edge" and the "Fe edge." Here, by "measured intensities" we mean normalized data from which S_{I} has been subtracted, as described in the text.

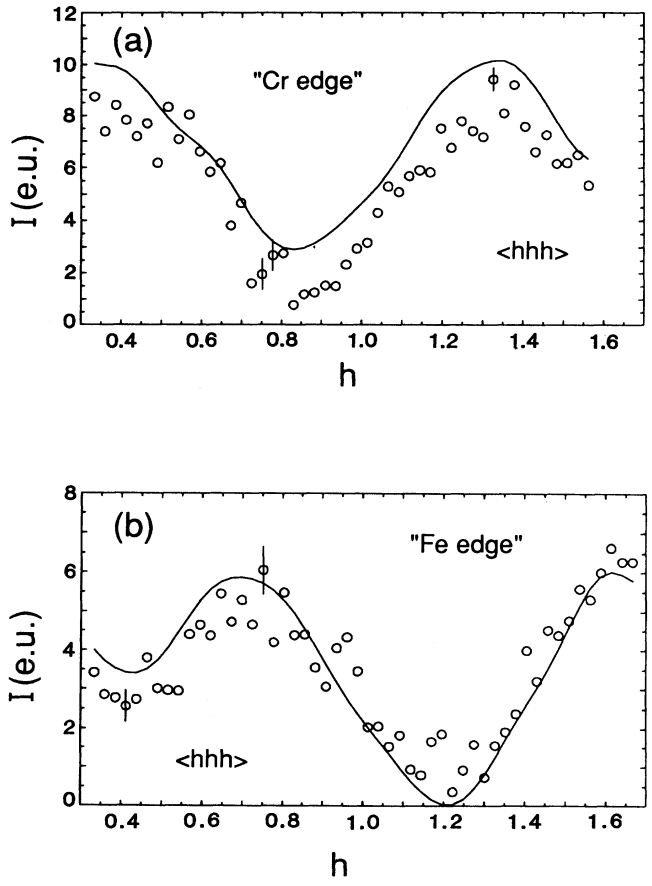

FIG. 7. Measured and reconstructed intensities in the $\langle hhh \rangle$ direction (again, S_{I} is removed). (a) "Cr edge," (b) "Fe edge."

E. Short-range order

The first eleven α_{lmn} in Table II (up to the 511 shell) are positive. This indicates a preference for like neighbors (Fe-Fe, Cr-Cr), i.e., a clustering tendency. For example, $\alpha_{111} \cong 0.16$ means that the probability of finding an Fe atom in the nearest-neighbor shell of another Fe atom is 60.5% as compared to 52.8% ($=c_{\mathrm{Fe}}$) in the case of total randomness. Given the high concentration of the sample, the α_{lmn} are rather small (the limiting value for complete phase separation is $\alpha_{lmn}=1.00$) and the clustering is not very pronounced. Our quench temperature is in fact well above the proposed metastable unmixing temperature $T_c \approx 850$ K.[2] However, for $T < T_\sigma \approx 1103$ K the σ phase is the equilibrium state (the sample concentration is in the homogeneity range of the σ phase[1]). According to anomalous x-ray diffraction studies by Yakel[43] σ-Fe-Cr is partially long-range ordered, i.e., there are sublattices (specified by the five nonequivalent positions in the σ unit cell) which are preferentially filled with Fe or Cr. For every interatomic vector connecting points in two different sublattices, the short-range order parameter will by necessity be negative. Evidently, the positive α_{lmn}'s of the bcc solid solution above T_σ do not reflect the chemical local order in the σ phase. The clustering along the $\langle 100 \rangle$ direction seems to be weaker than in other directions (α_{200}, α_{400}, α_{600} are all smaller than the average of their neighbors and α_{600} is the only significantly negative SRO parameter). However, this anisotropy is not very pronounced and the SRO intensity, reconstructed from the α_{lmn} exhibits a nearly isotropic maximum at the (000) position. The intensity at (000) is 4.9 Laue units, as compared to a constant intensity of 1 Laue unit for total randomness. To visualize the short-range ordered state a computer bcc crystal containing 64^3 atoms was fitted to the experimental short-range order parameters. All α_{lmn} of the model crystal were within the statistical error bars (Table II) of the experimental ones. In Fig. 8, a (110) plane of such a modeled crystal is shown along with one of a totally random alloy of identical composition. The clustered alloy clearly exhibits distinct Fe and Cr rich regions of substantially larger size than the Cr and Fe patches in the random configuration.

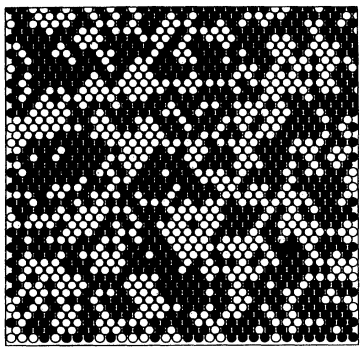

Actual (clustered)

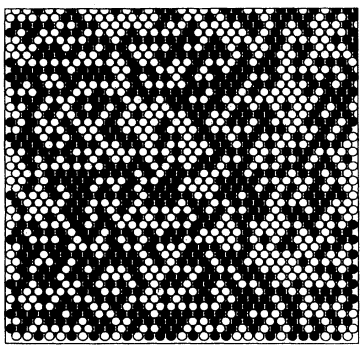

Random

FIG. 8. A(110) plane of both our clustered alloy and a random alloy with identical concentration modeled as described in the text (solid circles are Cr atoms).

F. Atomic displacements

The displacements parameters $\langle \mathbf{u}_l^{ij} \rangle$ are usually interpreted in terms of "bond lengths" between atomic species i and j:

$$R_l^{ij} = \frac{\langle \sigma_0^i \sigma_l^j | \mathbf{R}_l - \mathbf{w}_0^i + \mathbf{w}_l^j | \rangle}{\langle \sigma_0^i \sigma_l^j \rangle} \approx R_l + \frac{\mathbf{R}_l}{R_l} \cdot \langle \mathbf{u}_l^{ij} \rangle \ . \tag{29}$$

For example the average nearest-neighbor distance between two atoms i and j is given by

$$R_{111}^{ij} = \frac{\sqrt{3}}{2} a (1 + 2 \langle x_{111}^{ij} \rangle) \ . \tag{30}$$

(Note that in high symmetry cubic directions the average displacements are radial.) From Table III we see that most of the $\langle x_{lmn}^{\mathrm{FeFe}} \rangle$ are negative. Therefore most of the average Fe-Fe separations (in particular those for the first three shells) are smaller than the corresponding mean lattice distances. This is compatible with the observed decrease of the lattice parameter with increasing Fe concentration. However, the comparatively large *negative* value of the nearest-neighbor Cr-Cr displacement $\langle x_{111}^{\mathrm{CrCr}} \rangle$ shows that the concentration dependence of the lattice parameter is not necessarily reflected in a simple way in the local atomic distortions (from the above analogy one would expect a positive $\langle x_{111}^{\mathrm{CrCr}} \rangle$). Nevertheless, the $\langle x_{lmn}^{\mathrm{CrCr}} \rangle$ are on average more positive than the $\langle x_{lmn}^{\mathrm{FeFe}} \rangle$; i.e., the data suggests, taken over a sufficiently large local volume, that the Cr atom is "larger" than the Fe atom. The dominant displacements in Table III are those for the Cr-Cr pairs in the first and second neighbor shells, the Fe-Fe displacements being considerably smaller. The average Cr-Cr nearest-neighbor distance is 0.4% smaller and the average Cr-Cr next nearest-neighbor distance is 0.3% larger than the corresponding mean lattice separations. By comparison, the lattice parameter of *pure* Cr is 0.6% larger than the lattice parameter of *pure* Fe.

To our knowledge there exist no successful first-principles calculations of local atomic displacements in concentrated solid solutions. The theory of Froyen and Herring[44] considers an effective elastic medium, in which the initial force acting on an unrelaxed atom (sitting on a position of the periodic mean lattice $\mathbf{R}_m$) is related

linearly to the concentration fluctuations as in Krivoglaz[3] and Cook-de Fontaine:[45]

$$\mathbf{F}_m = \sum_n \mathbf{K}_{mn} \Delta\sigma_n^A \ . \tag{31}$$

The displacements in the relaxed configuration are then obtained from the force field using the dynamical matrix for the alloy crystal. For a numerical evaluation, Froyen and Herring assume a radial nearest-neighbor force $\mathbf{K}$ and a totally random alloy. [Since the correlations and the distortions in our sample are both rather weak, the assumption of total randomness and the use of the linearized expression (31) might well be thought to be justified.] The force $\mathbf{K}$ as well as the averages involving the dynamical matrix are then calculated approximately from da/dc and the elastic constants. Using the data for our sample, one obtains for the nearest-neighbor displacement parameters $\langle x_{111}^{\mathrm{FeFe}} \rangle = -0.000\,47$ and $\langle x_{111}^{\mathrm{CrCr}} \rangle = +0.000\,53$. Thus the Cr-Cr displacement parameter is positive. In fact, the theory presented in Ref. 44 cannot reproduce the experimentally observed negative signs of both $\langle x_{111}^{\mathrm{CrCr}} \rangle$ and $\langle x_{111}^{\mathrm{FeFe}} \rangle$, even if one were to use realistic values for the dynamical matrix (from the phonon dispersion curves) and a more sophisticated microscopic model for the $\mathbf{K}_{mn}$. This is because the basic assumption of species-independent forces in (31) leads to a displacement field given by Eq. (27) which is also independent of A and B. Assuming $\mathbf{w}_m^A = \mathbf{w}_m^B = \mathbf{w}_m$, one obtains from the definition (14) in the limit of vanishing correlations:

$$\langle x_{lmn}^{\mathrm{FeFe}} \rangle = -\frac{c_{\mathrm{Cr}}}{c_{\mathrm{Fe}}} \langle x_{lmn}^{\mathrm{CrCr}} \rangle \tag{32}$$

which is predicted by the Froyen-Herring theory. In order to describe the experimental findings in a linear theory one eventually has to introduce species-dependent forces $\mathbf{K}_{mn}^A, \mathbf{K}_{mn}^B$ or, equivalently, as an extension of Eq. (27):

$$\mathbf{w}_m^A = \sum_n \mathbf{A}_{mn}^A \Delta\sigma_n^A \ , \tag{33}$$

with an analogous expression for $\mathbf{w}_m^B$. Otherwise the Cook-de Fontaine treatment[45] suffers from a reduction in local information because it uses an average solute-lattice coupling together with an average lattice response function.

It is also important to note that, apart from any physical argument, the $\langle hhh \rangle$ size effect intensity discussed in Sec. IV D will depend on the symmetry of the bcc lattice much as with short-range order scattering. To illustrate this we consider the following sums which appear in the expression for the size effect intensity in Eq. (12). We shall discuss only nearest (NN) and next-nearest (NNN) neighbor terms:

$$\mathbf{Q} \cdot \sum_{\substack{\mathrm{NN} \\ \text{or NNN}}} \gamma_l e^{i\mathbf{Q}\cdot\mathbf{R}_l} \ , \tag{34}$$

where the NN terms include all 8 $\{111\}$ distances and NNN terms are the 6 $\{200\}$ distances. Taking positive values for the components of γ_{111} and γ_{200}, in the $\langle hhh \rangle$ direction the NN contribution has a maximum at $h \approx 0.82$ and a minimum at $h \approx 1.21$ whereas the NNN sum has a minimum at $h \approx 0.78$ and a maximum at $h \approx 1.27$. The actual minima and maxima in the size effect scattering will depend on the signs and relative magnitudes of γ_{111} and γ_{200}. In the present case the first two pairs of values in Table III give maxima at 0.82 and 0.78, respectively, for the "Fe edge" scan and minima at these places for the "Cr edge" scan. Were we to use the Froyen-Herring displacement parameters given above the profiles would be reversed, i.e., maxima would be minima at both edges in defiance of the data. It is also quite interesting that, by themselves, the signs of the dominant Cr-Cr displacements in the first two neighbor shells are essentially required by the observed sequence of maxima and minima along $\langle hhh \rangle$ in the two data sets.

This observation—that the negative Cr-Cr displacement in the nearest-neighbor shell is required by the $\langle hhh \rangle$ profile—does not, however, tell us why such an anomalous displacement prevails. For this we must defer both to the forces and to the response function of the crystal. The elastic softening near $\frac{2}{3}(111)$ and equivalent points is a property of the mean lattice in which Cr and Fe atoms reside. The displacements of these atoms depend not only on their sizes (the forces they exert) but also on this response. The size effect peaking then results from both the geometry of the bcc lattice and a set of accommodating displacements. Were the displacements to differ significantly from their measured values this accommodation would be accordingly less. Put another way the measured local displacements reflect in detail the values of $\mathbf{A}_{mn}^A$ and $\mathbf{A}_{mn}^B$ in Eq. (33) which in turn depend on both the response function of the crystal and the *individual* solute-lattice coupling parameters $\mathbf{K}_{mn}^A$ and $\mathbf{K}_{mn}^B$ as well as, implicitly, on the fact that the lattice is bcc.

G. Pair interactions

In thermal equilibrium, the correlations in an alloy are determined by the interactions between the different atoms. Since the measured SRO intensity reflects pair correlations, the information obtainable from a diffuse scattering experiment will be most probably confined to two-body interactions. Considering only pairwise interactions, one obtains an Ising-like Hamiltonian

$$H = H_0 + \tfrac{1}{4} \sum_{mn} V_{mn} \Delta\sigma_m \Delta\sigma_n \ , \tag{35}$$

where $\Delta\sigma_m = \sigma_m - \langle \sigma_m \rangle$ are the fluctuations of the spin variable $\sigma_m = 2\sigma_m^A - 1 = \pm 1$ and H_0 is the energy of the random alloy of the same concentration. The V_{mn} are the effective pair interactions:

$$V_{mn} = \tfrac{1}{2}(V_{mn}^{AA} + V_{mn}^{BB} - 2V_{mn}^{AB}) \ . \tag{36}$$

To solve the "inverse problem," i.e., to determine the effective pair interactions from the measured short-range order two methods were employed.

(i) The high-temperature ($V_{mn}/k_B T \ll 1$) mean field Krivoglaz-Clapp-Moss approximation[46,3] (KCM) yields

$$\alpha(\mathbf{q}) = \frac{D}{1 + \dfrac{2c_A c_B}{k_B T} V(\mathbf{q})} \ , \tag{37}$$

where $\alpha(\mathbf{q})$ and $V(\mathbf{q})$ re the Fourier transforms of the SRO parameters and the pair interactions. In calculating $\alpha(\mathbf{q})$ we used the α_I from Table II with α_{000} replaced by its theoretical value of 1, and set $D=1$ because it appears to yield the best agreement with the inverse Monte Carlo method.[47–49]

(ii) The inverse Monte Carlo method (IMCM)[47] is exact within the Ising model. (The "normal" Monte Carlo algorithm which is used to calculate the correlations from the interactions is also approximation-free.) The IMCM exploits the fact that in equilibrium the thermal fluctuations do not change the thermodynamic averages of observables (condition of detailed balance). The fluctuations are realized by virtual interchanges of A and B atoms in a computer-model crystal compatible with the measured SRO. The observables considered were the numbers of B—B bonds at a given distance $\mathbf{R}$. The principle of detailed balance yields nonlinear coupled equations for the V_{mn} because the probability of the fluctuation itself is a function of the energy change due to the fluctuation. In our calculations we used crystals with 64^3 atoms and considered $4\times 96\,000$ A-B exchanges to build the thermal averages.

It is interesting to compare our effective pair interactions which are primarily phenomenological parameters of a model Hamiltonian with the results of recent electronic first-principles band-structure calculations. In a recent study[50] the generalized perturbation method (GPM)[51] in conjunction with the KKR-CPA (Korringa-Kohn-Rostoker coherent-potential approximation[52]) was applied to equiatomic FeCr. In the GPM, the energy difference between the totally random alloy (as described by the CPA) and a given configuration is expanded in n-site interactions with pair interactions as lowest order terms [as in Eq. (35)]. The calculations in Ref. 50 were done for a nonmagnetic alloy, which should be appropriate for our sample, since the estimated magnetic $T_c\sim 540$ K[2] is well below the quench temperature.

The results of the IMCM and the KCM evaluations as well as of the calculations from Ref. 50 are listed in Table IV. All data sets show a dominant, negative nearest-neighbor interaction $V_{111}\approx -30$ meV. The negative sign of V_{111} indicates a clustering tendency, according to Eq. (36). Comparing the IMCM and the KCM results, one finds an excellent agreement; in fact, only the values for V_{111} differ noticeably. This is probably due to the fact that V_{111} is an appreciable fraction of the thermal energy: $|V_{111}|/k_BT\approx 0.39$ and therefore the mean-field assumptions of the KCM approximation are no longer fulfilled. The KKR-CPA-GPM results show a remarkable agreement with our data for the nearest neighbor and next-nearest neighbor distances. The values of V_{220}, V_{311}, and especially V_{222} show considerable deviation from the experimental values. This notwithstanding, the overall agreement is rather good. (See Ref. 53 for other comparisons of IMCM and KKR-CPA-GPM results.) Using the IMCM pair interactions in a Monte Carlo simulation,[54] we calculated the equilibrium short-range order at the quench temperature of our sample. Most of the obtained SRO parameters were within the 1σ error interval of the parameters in Table II, and all of them were within the 3σ error bar. Thus the Ising model gives an appropriate description of the atomic SRO in this alloy. (Note however, that the pair interactions in the α-Fe-Cr are strongly concentration dependent.[6])

TABLE IV. Pair interactions, V_{lmn} in meV.

lmn	inverse MC	Krivoglaz-Clapp-Moss	KKR-CPA-GPM (Ref. 50)
111	−27.2(3)	−28.2(3)	−29.5
200	3.6(3)	3.9(2)	4.2
220	0.6(1)	0.6(2)	4.8
311	−0.4(1)	−0.4(1)	3.2
222	0.3(1)	0.5(1)	−6.0
400	1.9(1)	1.8(1)	2.0
331	0.6(1)	0.6(1)	0.4
420	−0.2(2)	−0.2(1)	—
422	0.0(1)	0.0(1)	0.1
333	−0.1(1)	−0.1(1)	1.7
511	−0.3(1)	−0.3(1)	−0.2

H. Remarks on premonitory σ-phase fluctuations

What finally can be deduced about the σ-phase transformation from these results? The average structure of the σ phase in Fe-Cr has been determined by Bergman and Shoemaker[55] and the ordering has been investigated by Yakel[43] and Algie and Hall.[56] The σ phase (space group $P4_2/mnm$) has 30 atoms in the tetragonal unit cell, 22 of which are positioned on two Kagomé nets perpendicular to the tetragonal c axis at $z=0$ and $z=\frac{1}{2}$. These nets are rotated by 90° with respect to each other. The remaining 8 atoms per unit cell form two diamond nets at $z\approx\frac{1}{4}$ and $z\approx\frac{3}{4}$. Since the projection of the σ-phase structure in the $\langle 001\rangle_\sigma$ direction exhibits pseudohexagonal symmetry, this direction will most likely be related to the $\langle 111\rangle_{\rm bcc}$ in a displacive phase transformation. In the transformation scheme proposed by Kitchingman[57] three consecutive $(11\bar{1})$ planes of the bcc structure are moved along the $\langle 11\bar{1}\rangle$ direction to form two layers (one Kagomé and one diamond net) of the σ structure. The atoms in every second Kagomé layer have to undergo additional movements to generate the required rotations of the tilings. The orientational relations between the bcc and the σ structure for this model are $(001)_\sigma\|(11\bar{1})_{\rm bcc}$ and $\langle\bar{1}40\rangle_\sigma\|\langle 1\bar{1}0\rangle_{\rm bcc}$ with $a_\sigma=\sqrt{26/3}\,a_{\rm bcc}$ and $c_\sigma=\sqrt{3}\,a_{\rm bcc}$.

Using the above relationships we have calculated the bcc positions of several strong σ reflections from Ref. 55. There are only eleven of these σ reflections with bcc positions (or symmetrically equivalent bcc positions) that (a) were within our measured volume and (b) were located far enough from the bcc Bragg peaks to be observed. Only three of these reflections could be qualitatively associated with maxima in the diffuse scattering: the $(002)_\sigma$ and $(004)_\sigma$—corresponding to $\frac{2}{3}(111)_{\rm bcc}$ and $\frac{4}{3}(111)_{\rm bcc}$—and the $(413)_\sigma$, which is close to the $(210)_{\rm bcc}$. However, as discussed previously, the $\sim\frac{2}{3}(111)$ and $\sim\frac{4}{3}(111)$ maxima result from an intrinsic property of the bcc lattice and

are not uniquely related to the σ-phase formation although they are certainly required by it. Similarly, the maximum near (210) (visible in the "Fe edge" and the 7.6-keV data in Fig. 3) is related to a zone boundary softening of the $[100]_L$ phonon branch in our sample.[37] Such softening has been also observed[58] in the pure bcc metals Cr, Mo, and W and therefore cannot be regarded solely as a precursor of the bcc-σ transition.

Based on TEM and diffuse x-ray scattering studies on Mo-Re alloys Aparov *et al.*[59] proposed a different mechanism of the bcc-σ transformation. Their scheme implies $\langle 100\rangle_\sigma \| \langle 100\rangle_{\rm bcc}$, $\langle 010\rangle_\sigma \| \langle 010\rangle_{\rm bcc}$, and $a_\sigma = 3a_{\rm bcc}$. Two displacement waves with wave vectors from the $\frac{1}{6}\{420\}_{\rm bcc}$ star, each of them acting on only one sublattice, distort the bcc lattice to yield atomic arrangements which locally resemble those of the σ phase. However, we observed no diffuse maxima at $\frac{1}{6}(420)$ or equivalent positions and therefore no indication of precursors of this transformation mechanism in the Fe-Cr crystal.

V. CONCLUSIONS

We may conclude that our anomalous-scattering study has been largely successful in portraying the short-range order (clustering) in an $Fe_{0.53}Cr_{0.47}$ crystal including a satisfactory determination of pair interaction energies. The experimental techniques of Compton and RRS removal and zero-contrast subtraction (7.6-keV data) yielded consistent data sets that permitted an analysis of weak diffuse scattering that would otherwise be contaminated by parasitic scattering and swamped by the thermal diffuse contribution. Using both contrast enhancement and contrast variation to highlight the short-range order and size effect scattering we were also able to extract reliable values of the individual Cr-Cr and Fe-Fe local displacement parameters. These parameters are quite small because the size difference between pure Cr and Fe is only 0.6% which is one of the smaller differences in binary metallic solutions. However, as noted above, even though these displacements are small they reveal in detail a picture of the local atomic arrangements that demands more attention. In particular both nearest-neighbor Cr-Cr and Fe-Fe displacements are negative in clear disagreement, for example, with the Froyen-Herring treatment.

At first glance, a simultaneous decrease in both $\langle 111\rangle$ distances might be attributable to an ω-phase collapse as discussed in Sec. IV C. However, this ω instability is soft precisely because it leaves the $\langle 111\rangle$ nearest-neighbor bond length unchanged (it is really a zone boundary transverse $\frac{1}{3}\langle 112\rangle$ displacement). We have therefore had to resort to symmetry as well as elasticity in order to understand the $\langle hhh\rangle$ plots of short-range order and size effect scattering in Fig. 7. An ω-like softness may well underlie the distinctive features of these plots; but the size effect is an occupation/displacement correlation and not a pure displacement/displacement effect. Furthermore, while the $\frac{2}{3}(111)$ susceptibility is appreciable it is certainly not the sole contribution to the local displacement field.

We dwell on this $\frac{2}{3}(111)$ mode because it is involved directly in the σ-phase transformation as discussed earlier. However, we cannot otherwise detect any other premonitory signatures of the σ phase and we are left with the conclusion that, for this strongly first-order transformation, the precursor fluctuations are largely suppressed in the disordered bcc crystal. The pair interactions also appear to signal the onset only of (metastable) phase separation and not the incipient σ-phase ordering. In other words our experiment has proven to be rich in results pertaining to the bcc phase but not particularly instructive, thus far, on the σ-phase formation.

ACKNOWLEDGMENTS

This research was supported by the National Science Foundation Grant No. DMR-8903339. L.R. has been supported as well by the Schweizerischer Nationalfonds zur Förderung der wissenschaftlichen Forschung. This research was performed in part at the Oak Ridge National Laboratory beam line X-14 at the National Synchrotron Light Source, Brookhaven National Laboratory, sponsored by the Division of Materials Sciences and Division of Chemical Sciences, U.S. Department of Energy and under Contract No. DE-AC05-840R21400 with the Martin Marietta Energy System, Inc. We wish also to thank L. E. Tanner for providing our single crystal grown by L. L. Jones, P. E. A. Turchi for helpful discussions and for permitting our use of presently unpublished results, and S. Dietrich and P. Wochner for valuable insights into the scattering theory.

*Present address: Lawrence Livermore National Laboratory, L-268, P.O. Box 808, Livermore, CA 94550.

†Present address: National Institute of Standards and Technology, Reactor Building 235, Gaithersburg, MD 20899.

[1] O. Kubaschewski, *Iron Binary Phase Diagrams* (Springer, New York, 1982), and references therein.

[2] S. Hertzman and B. Sundman, CALPHAD **6**, 67 (1982).

[3] M. A. Krivoglaz, *The Theory of X-Ray and Thermal Neutron Scattering by Real Crystals* (Plenum, New York, 1969).

[4] B. E. Warren, *X-Ray Diffraction* (Addison-Wesley, Reading, MA, 1968).

[5] L. H. Schwartz, and J. B. Cohen, *Diffraction from Materials* (Springer, Berlin, 1987).

[6] I. Mirabeau, M. Hennion, and G. Parette, Phys. Rev. Lett. **53**, 687 (1984).

[7] M. Hennion, J. Phys. F **13**, 2351 (1983).

[8] For a prior reference on the application of this "zero contrast" technique to alloy diffuse scattering, see G. E. Ice, C. J. Sparks, and L. B. Shaffer, Bull. Am. Phys. Soc. **35**, 262 (1990).

[9] T. G. Ramesh and S. Ramaseshan, Acta Crystallogr. A **27**, 569 (1971).

[10] B. Borie and C. J. Sparks, Jr., Acta Crystallogr. A **27**, 198 (1971).

[11] S. Dietrich and W. Fenzl, Phys. Rev. B **39**, 8890 (1989).

[12]R. Kubo, J. Phys. Soc. Jpn. **17**, 1100 (1962).
[13]W. Schweika and H.-G. Haubold, Phys. Rev. B **37**, 3240 (1988).
[14]T. B. Wu, E. Matsubara, and J. B. Cohen, J. Appl. Crystallogr. **16**, 407 (1983).
[15]C. B. Walker and D. T. Keating, Acta Crystallogr. **14**, 1170 (1961).
[16]P. Georgopoulos and J. B. Cohen, J. Phys. Colloq. **12**, C7-191 (1977).
[17]R. O. Williams, Oak Ridge National Laboratory Report No. ORNL-4828, 1972 (unpublished).
[18]S. Dietrich and W. Fenzl, Phys. Rev. B **39**, 8873 (1989).
[19]M. Furusaka, Y. Ishikawa, S. Yamaguchi, and Y. Fujino, J. Phys. Soc. Jpn. **55**, 2253 (1986).
[20]A. Habenschuss, G. E. Ice, C. J. Sparks, and R. A. Neiser, Nucl. Instrum. Methods Phys. Res. A **266**, 215 (1988).
[21]G. E. Ice and C. J. Sparks, Nucl. Instrum. Methods Phys. Res. A **266**, 394 (1988).
[22]G. E. Ice and C. J. Sparks, Nucl. Instrum. Methods Phys. Res. A **291**, 110 (1990).
[23]C. J. Sparks, Phys. Rev. Lett. **33**, 262 (1974).
[24]A. F. Kodre and S. M. Shafroth, Phys. Rev. A **19**, 675 (1979).
[25]*International Tables for X-Ray Crystallography, Vol. III* (Kynoch, Birmingham, England, 1962).
[26]S. Sasaki, KEK Report No. 88-14, 1989 (unpublished).
[27]J. J. Hoyt, D. de Fontaine, and W. K. Warburton, J. Appl. Crystallogr. **17**, 344 (1984).
[28]P. Suortti, J. B. Hastings, and D. E. Cox, Acta Crystallogr. A **41**, 413 (1985).
[29]*International Tables for X-Ray Crystallography, Vol. IV* (Kynoch, Birmingham, England, 1974).
[30]G. A. Carlsson and C. A. Carlsson, Med. Phys. **9**, 868 (1982).
[31]F. Biggs, L. B. Mendelsohn, and J. B. Hann, At. Data Nucl. Data Tables **16**, 201 (1975).
[32]P. M. Platzman and P. A. Wolff, *Waves and Interactions in Solid State Plasmas,* in Solid State Physics Supplement 13, edited by H. Ehrenreich, F. Seitz and D. Turnbull (Academic, New York, 1973).
[33]H. Cole and B. E. Warren, J. Appl. Phys. **25**, 814 (1952).
[34]S. M. Shapiro, J. Z. Larese, Y. Noda, S. C. Moss, and L. E. Tanner, Phys. Rev. Lett. **57**, 3199 (1986).
[35]S. C. Moss, J. Phys. (Paris) Colloq. **38**, C7-440 (1977).
[36]D. de Fontaine, Acta Metall. **18**, 275 (1970).
[37]These neutron data have been taken on the BT4 triple-axis spectrometer of the National Institute of Standards and Technology in collaboration with D. A. Neumann. A comprehensive set of phonon branches has been measured and fit and will be reported separately along with selected elastic scans.
[38]A. Heiming, W. Petry, J. Trampenau, M. Alba, C. Herzig, and G. Vogl, Phys. Rev. B **40**, 11425 (1989); W. Petry, A. Heiming, and J. Trampenau, Mater. Res. Soc. Symp. Proc. **166**, 161 (1990).
[39]S. C. Moss, D. T. Keating, and J. D. Axe, in *Phase Transitions—1973,* Proceedings of the Conference on Phase Transitions and Their Applicatios in Materials Science, edited by H. K. Henisch, R. Ray, and L. E. Cross (Pergamon, New York, 1973), p. 179; J. D. Axe, D. T. Keating, and S. C. Moss, Phys. Rev. Lett. **35**, 530 (1975).
[40]Y. Yamada and K. Fuchizaki, Phys. Rev. B **42**, 9420 (1990).
[41]S. L. Quimby and P. M. Sutton, Phys. Rev. **91**, 1122 (1953).
[42]G. D. Preston, J. Iron Steel Inst. **124**, 99 (1931).
[43]H. L. Yakel, Acta Crystallogr. B **39**, 20 (1982).
[44]S. Froyen and C. Herring, J. Appl. Phys. **52**, 7165 (1981).
[45]H. E. Cook and D. de Fontaine, Acta. Metall. **17**, 915 (1969).
[46]P. C. Clapp and S. C. Moss, Phys. Rev. **142**, 418 (1966).
[47]V. Gerold and J. Kern, Acta Metall. **35**, 393 (1987).
[48]B. Schönfeld, L. Reinhard, G. Kostorz, and W. Bührer, Phys. Status Solidi B **148**, 457 (1988).
[49]I. V. Masanskii, V. I. Tokar, and T. A. Grischenko, Phys. Rev. B **44**, 4647 (1991).
[50]P. E. A. Turchi, M. Sluiter, and G. M. Stocks, Mater. Res. Soc. Symp. Proc. **213**, 75 (1991).
[51]F. Ducastelle and F. Gautier, J. Phys. F **6**, 2039 (1976).
[52]P. E. A. Turchi, G. M. Stocks, W. H. Butler, D. M. Nicholson, and A. Gonis, Phys. Rev. B **37**, 5982 (1988).
[53]M. Sluiter, P. E. A. Turchi, D. D. Johnson, F. J. Pinski, D. M. Nicholson, and G. M. Stocks, Mater. Res. Soc. Proc. **166**, 225 (1990); P. E. A. Turchi, F. J. Pinski, R. H. Howell, A. L. Wachs, M. J. Fluss, D. D. Johnson, G. M. Stocks, D. M. Nicholson, and W. Schweika, *ibid.* **166**, 225 (1990).
[54]K. Binder, in *Monte Carlo Methods in Statistical Physics,* edited by K. Binder (Springer, Berlin, 1979), p. 1.
[55]G. Bergman and D. P. Shoemaker, Acta Crystallogr. **7**, 857 (1954).
[56]S. H. Algie and E. O. Hall Acta Crystallogr. **20**, 142 (1966).
[57]W. J. Kitchingman, Acta Crystallogr. A **24**, 282 (1968).
[58]J. D. Axe, in *Electron-Phonon Interactions and Phase Transitions,* edited by T. Riste (Plenum, New York, 1977), p. 50.
[59]N. N. Aparov, I. V. Lyasotskiy, Yu. D. Tyapkin, and V. Ye. Panin, Fiz. Metal. Metalloved. **40**, 354 (1975) [Phys. Met. Metallogr. (USSR) **40**, 107 (1975)].